Journal of the Chinese Institute of Engineers, Vol. 26, No. 4, pp. 481-491 (2003)

TRACKING THE RADIOMETRIC PERFORMANCE OF THE ROCSAT-1 OCEAN COLOR IMAGER

Wei-Song Lin* and Wen-Hao Sung

ABSTRACT

The Ocean Color Imager (OCI) is a multispectral imaging sensor aboard the ROCSAT-1 satellite with seven charge-coupled device (CCD) linear arrays as optical detectors. The CCD is known to be vulnerable to radiation damage, and optical transmission decays due to long-term exposure to the space environment. The radiometric performance of OCI in-orbit is therefore subject to change and tracking its performance becomes necessary. In this paper, a linear model characterizes the radiometric response of each OCI pixel and the performance tracking is achieved by studying the model parameters (gain and offset). The model parameters are basically a combination result of the component response functions associated with the optical and electronic components. Dark measurement and calibration with an integrating sphere referring to a copper-point blackbody source obtained the initial offsets and gains, respectively. The in-flight offsets are estimated by statistically analyzing the night measurement data, and the results obtained by tracking for twenty-three months show a gradual increase. A track differential radiance method is developed for performing in-flight cross platform comparison to estimate the gain shift. The experiment compares the radiance data acquired by OCI and SeaWiFS over cross points near in time. The results show the gains are stable.

Key Words: ocean color, OCI, radiometric performance, radiation damage.

I. INTRODUCTION

The Ocean Color Imager (OCI) aboard the ROCSAT-1 satellite, launched on Jan. 26th 1999 and still on duty in May 2002, is a pushbroom scanner with six plus one spectral bands (including a duplicate for backup) for measuring water-leaving radiance from low-latitude oceans (altitude 600km, inclination 35 degrees) to contribute an understanding of ocean dynamics, chlorophyll variation, and oceanic primary production. The OCI is an all-refractive, nadir-viewing optical instrument with charge coupled-device (CCD) linear arrays as the detectors of each band (Lin *et al.*, 1999). The CCD device, TH7811 (Thomson-CSF) linear CCD array, is composed of 1728 cells of photosensitive area, and for each band, the cells are organized into 896 image pixels with 64 single-cell pixels located centrally and 832 double-cell pixels separated equally on both sides. The Ground-Instantaneous-Field-of-View (GIFOV) of double and single cell pixels at nadir on a 600km orbit are approximately 800m and 400m, respectively. The radiance signal measured by each pixel is digitized into 12-bit numbers. The spectral bands, listed in Table 1, were selected in the visible and near infrared regions corresponding to chlorophyll absorption and aerosol correction and matching six of the SeaWiFS (aboard SeaStar satellite produced by NASA) bands centered at 443, 490, 510, 555, 670, and 865 nm, respectively (Hooker *et al.*, 1992). The seven CCD arrays of OCI are assembled, respectively, on seven different focal planes accommodated by four independent telecentric dioptric systems. Fig. 1 shows one of the telecentric dioptric systems with two focal planes. The overall response of each sensing pixel is actually a combination result of the component response functions associated with

---

*Corresponding author. (Tel: 886-2-23635251 ext. 413; Fax: 886-2-23638247; Email: weisong@cc.ee.ntu.edu.tw)

The authors are with the Department of Electrical Engineering, National Taiwan University, Taipei, Taiwan 106, R.O.C.

Table 1 Bands of OCI and SeaWiFS

OCI Band No.	SeaWiFS Band center(nm)	Band width (nm)	Phenomenon studied with OCI
	412	20	
1	443	20	Chlorophyll Absorption (blue)
2	490	20	Pigment
3	510	20	Chlorophyll Absorption (green)
4/7	555	20	Hinge point, Sediments (yellow)
5	670	20	Aerosol Correction (red)
	765	40	
6	865	40	Aerosol Correction (NIR)

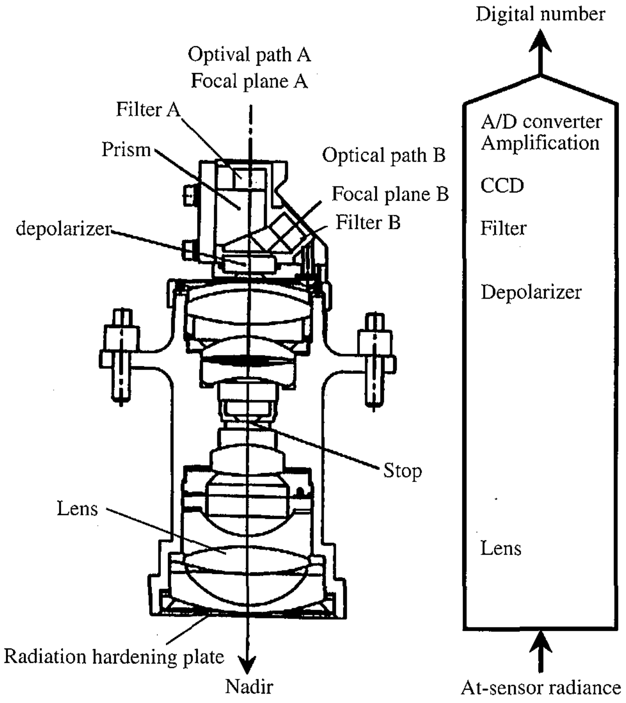

Fig. 1 A telecentric dioptric system of OCI with two focal planes, the right side shows its signal flow

the optics, detector, and electronics as indicated on the right of Fig. 1. The major factors affecting the gain and offset are the optical transmission, modulation transfer function, field-of-view, straylight, depolarization, and center wavelength and bandwidth of the filter in the optics, and the responsivity and dark current in the CCD, the amplification/attenuation, bias, quantization, sampling rate and noise in the analog and digital electronics.

The information containing radiance backscattered out of the water and transmitted to the top of the atmosphere is only a small portion of the total radiance measured by OCI (Gordon, 1998; Schowengerdt, 1997). To calculate the water-leaving radiance, the OCI data beamed down requires several levels of radiometric calibration. The sensor calibration (calibration-to-radiance) converts the measured digital number to the at-sensor radiance, the atmospheric correction transforms the at-sensor radiance to the radiance at the ocean surface, and the surface correction removes the radiance reflected directly from the ocean surface. To achieve the calibration-to-radiance, the scientist needs to have the models and associate pre- and in-flight parameters to describe the optical response of each pixel (Rao and Chen, 1994). A linear model has been used to characterize the optical response for the OCI applications and the pre-flight model parameters were obtained by calibration with respect to an integrating sphere referring to a copper-point blackbody source or shutting off the aperture (Narimatsu *et al.*, 1997b). However, the gain associated with each sensing pixel represents, actually, a combination of the spectral, spatial and electronic response functions of the associated components along the signal path (optical and electronic). Any performance degradation or damage in a component may result in the gain deviating from its original design. Unfortunately, the continuous bombardment of high-energy particles in the space environment has always been found to result in damage in the lens, CCD, and analog electronic devices (Yamashita *et al.*, 1997). Conventionally, an on-board calibrator such as a blackbody source, a reference lamp or diffused sunlight is invoked to calibrate the gain in-orbit (Ono *et al.*, 1996; Rao and Chen, 1994). But the compact design of OCI with nearly a thousand pixels in a band makes it very difficult and expensive to adopt such on-board calibrators. Considering such situations, vicarious calibration using reflectance- or radiance-based methods becomes the most appropriate solution (Gordon, 1998; Slater *et al.*, 1987). Fortunately, OCI is designed to match six of the eight ocean color bands of SeaWiFS, and makes it possible to do vicarious calibration to the gains with respect to the calibrated SeaWiFS data at cross points. This paper develops a track differential radiance method to implement the cross platform comparison for such vicarious calibration. Images taken from three cross points of these two sensors are compared and the results are presented.

In the space environment, trapped and flare protons have energies of up to million electronic volts and are very penetrating and cannot be effectively shielded against. Proton-induced radiation damage to the CCD may produce transient signal charge and permanent introduction of bulk damage, which generate dark current and trap signal charges (Hopkinson *et al.*, 1996). The dark current dominates the offset and its change in the linear model, surely the threshold voltage in the analog electronic circuit such as an amplifier/buffer also contributes to the offset. Technically, the offset can be measured easily by shutting off the light incident upon the aperture; however, a shutter is not available for OCI. We alternatively use dark night measurements and estimate the offsets statistically. The results obtained by tracking the OCI measurements for twenty-three months are shown.

The rest of the paper is organized as follows. The linear model and pre-flight parameters of OCI are presented in Section II. Using the dark night measurement data, the long-term variation of the offset is investigated in Section III. Section IV proposes the track differential radiance method and demonstrates the results of calibrating the gains by cross platform comparison. Concluding remarks are finally made in Section V.

II. LINEAR MODEL AND PRE-FLIGHT PARAMETERS OF OCI

The spectral response at pixel i in scan line j of an OCI band is theoretically the convolution of the component response functions, however with linear approximation, it is assumed to be an average value over an effective spectral band and area corresponding to the pixel (Schowengerdt, 1997). In this case, the band- and space-integrated at-sensor radiance measured by the pixel can be represented by

$$L_{ij} = \iiint_{\Delta y \Delta x \Delta \lambda} L_{ij}(\lambda, x, y)\, d\lambda\, dx\, dy \qquad (1)$$

where L_{ij} denotes the radiance, $\Delta\lambda$ is the effective spectral band, and $\Delta x \times \Delta y$ is the effective area. The linear model that relates the radiance to the measured digital number is described as

$$N_{ij} = \alpha_{ij} g_j F_{ip} L_{ij} + D_{ij} \qquad (2)$$

and

$$\alpha_{ij} = \frac{F_{ij}}{F_{ip}} \qquad (3)$$

where the subscript p denotes a pre-flight term, N and D denote, respectively, the digital number and offset, g and α represent the amplification and relative gain, respectively, the gain (overall) is represented by the combination term, $\alpha_{ij} g_j F_{ip}$, and F_{ij} is a value representing the combination of the spectral and spatial responses of OCI. Since the amplification, g, which can be chosen either as low (0.5), normal (1.0) or high (2 or 6 for Band 6) is controlled by ground command, based upon the pre-flight values, the relative gain is the only one in the gain term to be calibrated in-orbit.

Using (2) and (3) to convert a digital number, N_{ij}, to the corresponding at-sensor radiance, L_{ij}, one needs to know the associated gain and offset. The pre-flight gain (α_{ij}=1.0) was measured in Oct. 1997 for normal amplification (g_j=1.0) with respect to an integrating sphere and a copper-point blackbody source at 1084.62°C as the primary standard of radiance (Narimatsu *et al.*, 1997b). Linear regression to the results of eight testing points approximated the pre-flight gain of each pixel (Lin *et al.*, 1999; Narimatsu and Watanabe, 1997a). The offset was measured by shutting off light incident upon the aperture while the CCD was being controlled at normal operating temperature (10±3°C) and at room temperature, respectively. The results associated with pixels 1, 416 and 896 of each band are listed in Table 2 (The other pixels are not presented). The significant difference between the offsets measured at two different temperatures confirms the dark current of the CCD being thermal sensitive, however the change in temperature seems to have little effect on the gain.

III. RADIATION DAMAGE EFFECTS INCREASING THE OFFSETS

The offset in the linear model represents mainly the CCD dark current that may be changed by thermal generation and proton-induced displacement damage. Thermal generation represents a process of the electrons or holes making transitions by absorbing thermal energy from high-energy particles. This process provides an undesired source of charge carriers, which cannot be distinguished from the photo-generated carriers. In a CCD device, electrons and holes are thermally generated in the depletion region; therefore cooling of a CCD device is a possibility for decreasing the dark current to a suitable value (Amelio and Dyck, 1975). For OCI, heater and radiator maintain the temperature of each CCD device at 10±3°C. Normally no heat accumulation may occur in CCD devices, and change in the offset due

Table 2 The pre-flight gain and offset of pixel 1, 416 and 896 (1997-10, g=1.0)

Band	CCD	Pixel no. 1		Pixel no. 416		Pixel no. 896	
	°C	F	D	F	D	F	D
1	30.7	21.27	85.22	25.50	87.63	20.45	84.85
	10.1		48.10		47.98		47.98
2	31.3	27.28	94.70	33.35	103.28	27.03	93.30
	9.9		47.63		47.65		47.43
3	28.4	31.84	91.80	38.54	98.25	31.24	88.20
	10.5		48.48		48.03		47.83
4	31.4	28.72	94.09	35.89	95.78	28.14	92.59
	10.0		47.73		47.48		47.48
5	28.8	69.07	90.99	85.86	90.67	70.65	85.27
	10.0		46.95		44.60		46.40
6	28.8	126.05	83.10	155.28	87.21	122.69	75.78
	9.7		46.70		46.48		45.98
7	29.6	32.91	84.89	40.40	87.99	30.64	81.79
	10.0		44.10		43.85		43.73

to temperature shift should be limited in amount. On the other hand CCD devices are radiation sensitive and especially vulnerable to effects due to protons that exist in the Earth's trapped radiation belts or arise from solar flares. When protons or other particles pass through semiconductor material, a smallfraction of energy may go into the displacement of atoms from their lattice sites and create crystal lattice defect energy levels in the energy gap of the semiconductors (Hopkinson *et al.*, 1996). These levels give an increased probability that a valence band electron will make a transition to the conduction band by proton or photon absorption. As a result the dark current in the CCD would have a higher current density owing to the larger density of the defects decreasing the minority carrier lifetime (Yamashita *et al.*, 1997). The continuous exposure of the CCD to environmental radiation will surely change its performance, and the bulk damage resulting from radiation is accumulative. Tracking the long-term offsets of OCI may reveal the effect.

Since no design exists for OCI to shut off the light incident upon its aperture, alternatively we turn to estimate the in-flight offset by statistically analyzing the dark night measurement data. Here dark night means a local night without moonlight. For a dark night measurement, the at-sensor radiance observed by OCI is assumed to be nearly zero or $L_{ij}\approx 0$ in (2). The offset can therefore be studied by setting $N_{ij}\approx D_{ij}$. However, considering the corruption of noise, the offset associate with a pixel is estimated as averaged over an image as

$$\overline{D}_i = \frac{1}{J}\sum_j N_{ij} \tag{4}$$

where J is the total number of scan lines taken into account. The band-mean offset is calculated as

$$\overline{D} = \frac{1}{IJ}\sum_i \sum_j N_{ij} \tag{5}$$

where I denotes the number of pixels in a scan line taken into account.

To collect the dark night measurement data sets, the criterion is that the band-mean offset (5) should be the smallest in a month. Then, from March 1999 till December 2000, thirty data sets are picked from more than one hundred and twenty sets of night measurement data. The band-mean offset and standard deviation are then calculated for each month. Table 3 compares the early flight values (April, 1999) with the pre-flight ones. In April 1999, OCI had been in-orbit for almost three months, a little increase that occurred in the band-mean offset as shown in Table 3 is valid, and the applicability of estimating the offset by using dark night measurement is verified. Using least square error approximation, the band-mean offsets with respect to time (days since launched) are approximated by linear equations. Table 4 shows the results, where y is the digital number and x is the number of days since OCI was launched (For example, x=1 and x=339 correspond to January 28, 1999 and January 1, 2000, respectively). The slope of each linear equation reveals the tendency and rate of the offset change. Positive slope appearing in each linear equation shows that each band-mean offset is increasing gradually along with the increase of operation time. At the end of the second year of operation, the offset of each pixel was found to have increased approximately 30%. It was also found that the

Table 3 Comparing the band-mean offsets, pre-flight and 1999-4. ($\overline{D}$ =mean offset, σ=standard deviation)

Band	Pre-flight				April 1999 (NI-A Mode)			
	Double-cell		Single-cell		Double-cell		Single-cell	
	$\overline{D}$	σ	$\overline{D}$	σ	$\overline{D}$	σ	$\overline{D}$	σ
1	47.98	0.29	42.20	0.33	48.53	0.45	42.58	0.79
2	47.98	0.29	42.20	0.33	48.98	0.46	42.98	0.76
3	47.53	0.35	42.13	0.43	48.44	0.50	42.51	0.79
4	48.19	0.32	42.32	0.22	48.41	0.43	42.53	0.75
5	47.01	0.22	39.66	0.30	46.24	0.27	35.91	0.69
6	46.80	0.18	41.49	0.22	46.38	0.22	40.21	0.41
7	45.30	0.25	39.31	0.27	NA	NA	NA	NA

Table 4 Linear interpolation to the band-mean offsets

Band	Double-cell	Single-cell
1	y=0.0203x+47.52	y=0.0107x+41.81
2	y=0.0220x+47.63	y=0.0119x+41.92
3	y=0.0233x+47.15	y=0.0121x+41.67
4	y=0.0127x+47.77	y=0.0066x+42.03
5	y=0.0219x+45.82	y=0.0130x+37.61
6	y=0.0265x+45.95	y=0.0145x+40.46
7	y=0.0228x+44.66	y=0.0115x+39.01

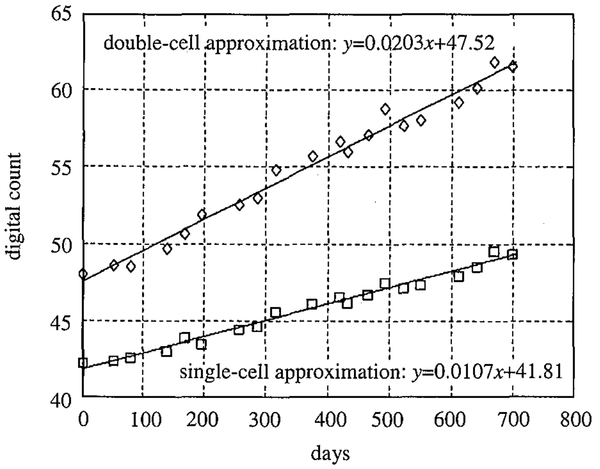

Fig. 2 Linear approximation to the band-mean offsets of Band 1, diamond: double-cell, square: single-cell

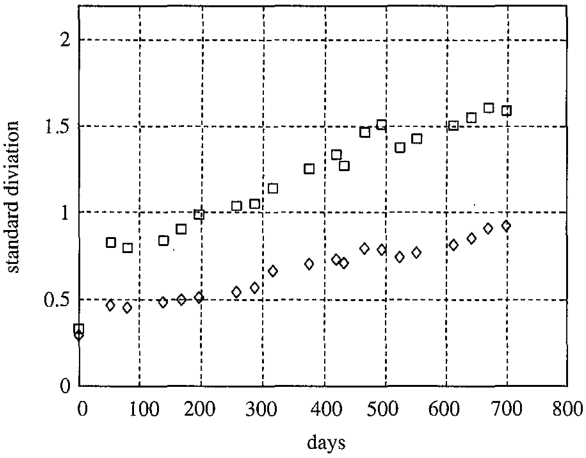

Fig. 3 Standard deviations of Band 1, diamond: double-cell, square: single-cell

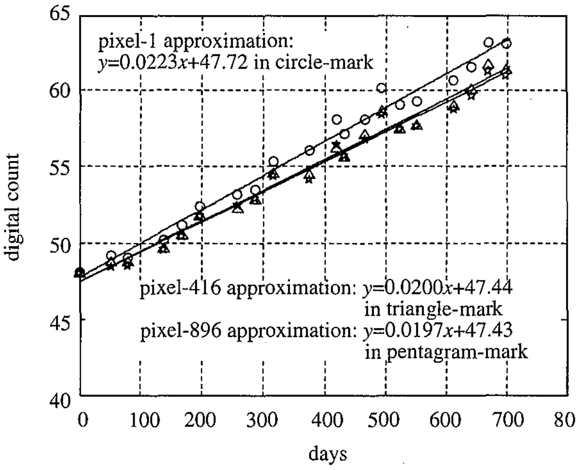

Fig. 4 Linear approximation to the mean offsets of pixels 1, 416, and 896 of Band 1

standard deviation, which indicates the random fluctua-tion, becomes larger with the increase of the band-mean offset. Figs. 2 and 3 show, respectively, the two-dimensional plots of the band-mean offset and standard deviation of Band 1 where double-cell pixels are marked with diamond shapes and single-cell ones are marked with squares (the other bands are not shown). Figs. 4 to 10 show the results of linear approximation to the mean offsets of pixels 1, 416, and 896 (double-cell pixels) of each band. All of these results confirm that, due to radiation damage, the offset or equivalently the dark current of each CCD

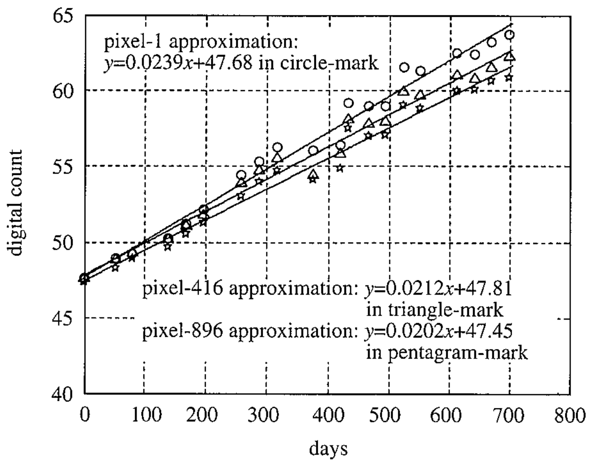

Fig. 5 Linear approximation to the mean offsets of pixels 1, 416, and 896 of Band 2

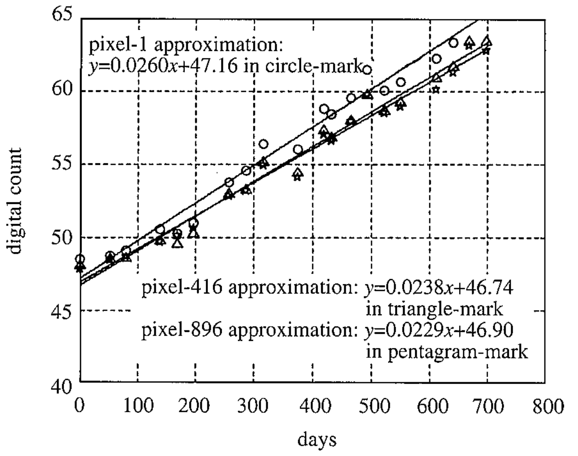

Fig. 6 Linear approximation to the mean offsets of pixels 1, 416, and 896 of Band 3

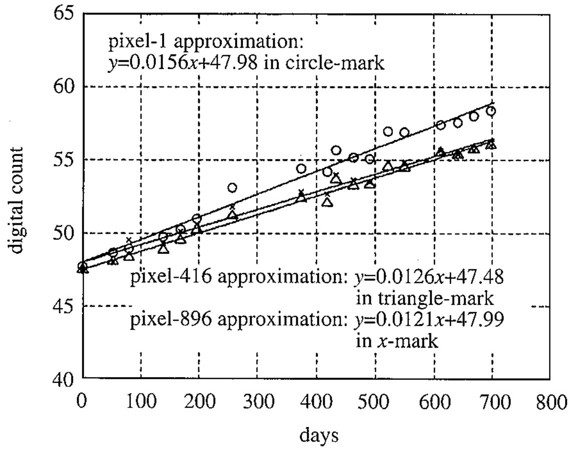

Fig. 7 Linear approximation to the mean offsets of pixels 1, 416, and 896 of Band 4

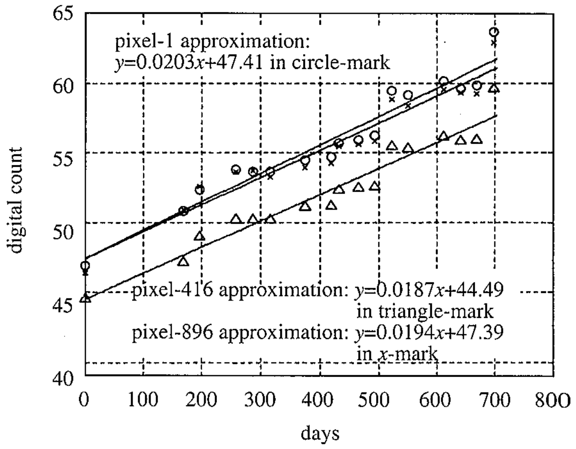

Fig. 8 Linear approximation to the mean offset of pixels 1, 416, and 896 of Band 5

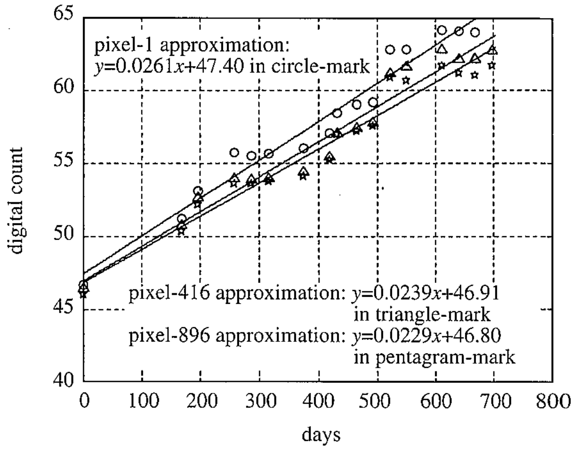

Fig. 9 Linear approximation to the mean offset of pixels 1, 416, and 896 of Band 6

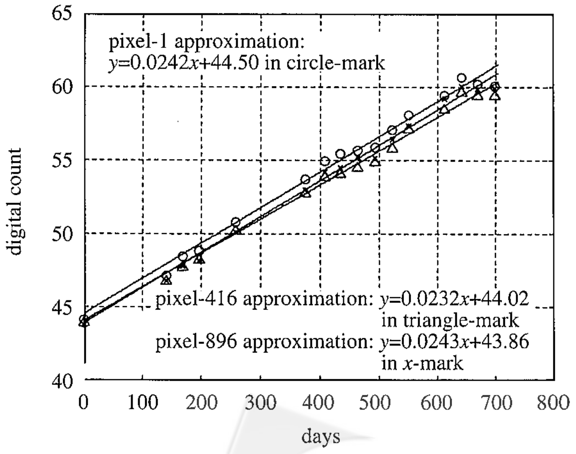

Fig. 10 Linear approximation to the mean offset of pixels 1, 416, and 896 of Band 7

pixel and its random fluctuation are gradually increasing. This fact will actually be a restriction on the lifetime of OCI.

IV. TRACKING THE GAIN SHIFT BY CROSS PLATFORM COMPARISON

1. Estimating the Relative Gain

Theoretically, if the offset has been calibrated and the at-sensor radiance, L_{ij}, is known either by measuring with a vicarious sensor or providing the radiance with a known source such as lamp light, blackbody radiator, moonlight or diffused sunlight (Ono *et al.*, 1996), the relative gain can be recovered from (2) as

$$\alpha_{ij} = \frac{N_{ij} - D_{ij}}{g_j F_{ip} L_{ij}} \tag{6}$$

Empirically, estimating the at-sensor radiance by vicarious measurements of the reflectance or radiance of some target site has been used with great success. Here, OCI has spectral bands matching six of the eight SeaWiFS bands and their lifetimes in orbit overlap (Hooker *et al.*, 1992; Salomonson *et al.*, 1989). This allows the possibility to calibrate the relative gain of OCI by referring to the calibrated SeaWiFS data over cross points. However, cross platform comparison has difficulties resulting from radiometric incompatibility, data set registration, and differences in spectral matching, ground spatial resolution, and sun-sensor geometry (Che *et al.*, 1991). To solve these difficulties, we put constraints on the data acquisition and use the track differential radiance method presented later instead of using (6) directly. The concepts are explained as follows:

Spectral matching: To reduce the uncertainties in spectral mismatch, SeaWiFS that has six bands nicely matching each OCI band is chosen for the cross platform comparison. *Ground spatial resolution:* The GIFOV of OCI and SeaWiFS are very different. To account for the difference of ground spatial resolutions of different sensors, cross comparison is done on the data acquired over the same ground coverage by organizing multiple GIFOV and re-sampling. *Sun-sensor geometry:* Sensors on different platforms will observe a target site under different illumination and viewing conditions that introduce atmospheric changes and surface bi-directional reflectance effects. The OCI orbit inclines 35° and has a ground track crossing that of a sun-synchronous orbit such as SeaWiFS. To reduce the effect of different sun-sensor geometry, the cross platform comparison considers merely the data obtained nearly at the same time over the cross points. *Radiometric incompatibility:* The radiometric responses of OCI and SeaWiFS were calibrated in the laboratory using known sources of spectral radiance such as integrating spheres and blackbody radiators. These sources referred to some primary standards maintained respectively by the United States and Japan. The differences in the instrumentation and calibration may ultimately cause OCI and SeaWiFS to show unequal radiance data when measuring the same at-sensor radiance. Technically the information of data incompatibility can be obtained by doing cross calibration before launch, but unfortunately the opportunity was lost. When measuring the same target at the same time, OCI and SeaWiFS should obtain compatible reflectance data at the same orbit position. The cross platform comparison can find the relative gains of OCI covering the incompatibility and gain shift. *Data set registration:* The cross platform comparison requires data sets over the cross point of ground tracks of OCI and SeaWiFS. To obtain the data set, usually both image and data set registrations are required. The image registration is achieved by mapping the two images onto one coordinate system based on the longitude and latitude. The concerned data sets are then picked from the overlapping area with the same ground coverage.

2. The Track Differential Radiance Method

Let the track of an OCI pixel over a target site be divided into segments R_a and R_b. Then, for pixel i and from (2), the single-track differential radiance $\tilde{L}_i$ is calculated as

$$\tilde{L}_i = \frac{\left| N_{ia} - N_{ib} \right|}{\alpha_i g F_{ip}} \tag{7}$$

where a and b denote terms in track segments R_a and R_b, respectively, and as a track segment contains multiple GIFOV, N_{ia} and N_{ib} are each taken as the average. Since N_{ia} and N_{ib} are measured by the same CCD detector, the offset is considered to be unchanged. Therefore the offset terms are eliminated from (7). This allows, if the track differential radiance is known, the relative gain to be calculated as

$$\alpha_i = \frac{\left| N_{ia} - N_{ib} \right|}{g F_{ip} \tilde{L}_i} = \frac{\tilde{L}_{ip}}{\tilde{L}_i} \tag{8}$$

where no calibration of the offset is required, and

$$\tilde{L}_{ip} = \frac{\left| N_{ia} - N_{ib} \right|}{g F_{ip}} \tag{9}$$

Considering providing the track differential radiance with the calibrated SeaWiFS data, the difficulty in data set co-registration and corruption of noise make the single track based calculation with (8) practically less reliable. Instead, the average of multiple tracks of differential radiance over the target site is used, and in this case (9) becomes

$$\tilde{L}_p = \frac{1}{I}\sum_{i=1}^{I} \frac{|N_{ia} - N_{ib}|}{gF_{ip}} \tag{10}$$

where I is the number of tracks (pixels) taken into account. The gain index, α_{index}, instead of the relative gain, is calculated as

$$\alpha_{index} = \frac{\tilde{L}_p}{\tilde{L}} \tag{11}$$

where $\tilde{L}$ is the track differential radiance to be provided by the SeaWiFS data. Obviously, the gain index is not guaranteed to be equal to a relative gain, but it can indicate the average behavior of the gain.

3. Getting the Track Differential Radiance from the SeaWiFS Data

The total at-sensor radiance of band λ arriving at a spaceborne sensor contains three significant components (Schowengerdt, 1997): the surface-reflected radiation, L^u, the surface-reflected skylight, L^d, and the up-scattered path radiance, L^p as

$$L(x, y)=L^u(x, y)+L^d(x, y)+L^p \tag{12}$$

or

$$L(x, y) = \rho(x, y, \lambda) = \frac{\tau_v(\lambda)}{\pi}\begin{Bmatrix} \tau_s(\lambda)E^0\cos[\theta(x, y)] \\ + T(x, y)E^d \end{Bmatrix} + L^p \tag{13}$$

where $\rho(x, y, \lambda)$ is the diffuse spectral reflectance, $\tau_v(\lambda)$ is the view path transmittance, $\tau_s(\lambda)$ is the solar path atmospheric transmittance, E^0 is the spectral irradiance at the top-of-the-atmosphere, $T(x, y)$ is the topological factor of the pixel, and E^d is the irradiance at the earth's surface due to skylight.

For a short time interval of measurement over a sufficiently small target site of ocean surface under steady atmospheric conditions, the view angles, view paths, view path transmittance, solar path transmittance, and the direct solar and skylight irradiance are approximately constant values. Then we can assume

$$\tau_s(b)E^0\cos[\theta(x, y)]+T(x, y)E^d=\text{constant} \tag{14}$$

and the track differential radiance is obtained as

$$\tilde{L} = |L_a - L_b| = \frac{\tau_v(\lambda)}{\pi}\begin{Bmatrix} \tau_s(\lambda)E^0\cos[\theta(x, y)] \\ + T(x, y)E^d \end{Bmatrix} \cdot |\rho_a(\lambda) - \rho_b(\lambda)| \tag{15}$$

where the terms with subscript a or b represent averages corresponding to R_a and R_b. The significant meaning of (15) is that the up-scattered path radiance terms, L^P, that is a combination of molecular Rayleigh scattering and aerosol and particulate Mie scattering are cancelled. This allows the data processing for in-flight calibration based on the track differential radiance to skip the requirement of atmospheric correction that is usually empirical and uncertain (Gordon, 1998). However, to achieve significant track differential radiance, the target site should be chosen with reflectance in R_a different from that in R_b. This will technically restrict the application of the method to calibrate every pixel.

Let OCI and SeaWiFS measure over the same target site nearly at the same time and within a limited range of view angles (≤30°) such that the Lambertian property applies approximately. Then, from (15), the track differential radiances arriving at each of them are different only by the view path transmittances or

$$\frac{\tilde{L}^{OCI}}{\tilde{L}^{SWF}} = \frac{\tau_v^{OCI}(\lambda)}{\tau_v^{SWF}(\lambda)} \tag{16}$$

where the superscripts OCI and SWF denote the terms associated with OCI and SeaWiFS, respectively, if the atmosphere along the view paths of the two sensors is homogeneous in scattering the solar radiation, and since the altitudes of OCI and SeaWiFS are 600km and 705 km, respectively. By measuring the same target at the same time, the lengths of both view paths within the atmosphere are almost equal and their view path transmittances can be assumed to be approximately the same. From (16), the track differential radiance observed by SeaWiFS is then equivalent to an OCI observation. Referring to the SeaWiFS measurement, (8) and (11), it seems that the relative gain and gain index can be calculated substitutively as

$$\alpha_i = \frac{\tilde{L}_{ip}}{\tilde{L}_i} = \frac{\tilde{L}_{ip}}{\tilde{L}_i^{SWF}} \tag{17}$$

and

$$\alpha_{index} = \frac{\tilde{L}_p}{\tilde{L}} = \frac{\tilde{L}_p}{\tilde{L}^{SWF}} \tag{18}$$

Table 5 The three OCI data sets for cross comparison

No.	Data Set	Longitude	Latitude	G.M.T.
1	e99159090959L11N16.L1A	32.4~55.14	-12.35~-28.9	09:10~09:16
2	e99292015800L11N16.L1A	145.8~166.7	34.63~21.3	01:58~02:03
3	e99340074730L11N16.L1A	57.1~66.55	14.1~4.32	07:47~07:49

Table 6 The three SeaWiFS data sets for cross comparison

No.	Data Set	Longitude	Latitude	G.M.T.
1	S1999159091051.L1B	7.8~59.09	-4.9~-53.9	09:11~09:23
2	S1999292015126.L1B	138.7~-160.5	65.47~19.4	01:51~02:03
3	S1999340074419.L1B	47.6~90.5	40.1~-2.4	07:44~07:55

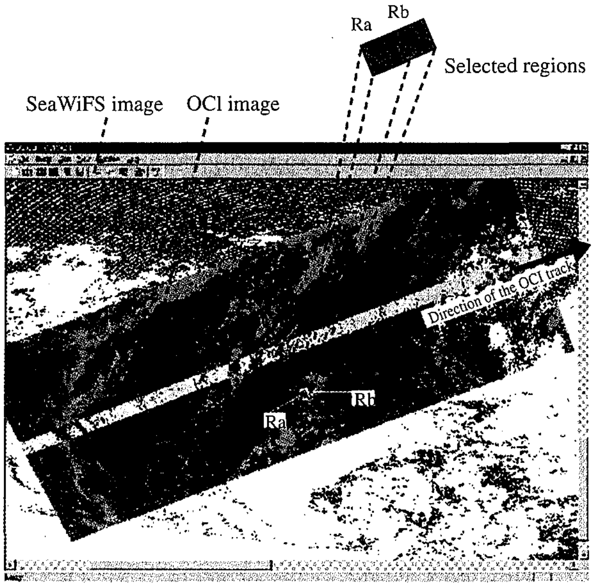

Fig. 11 Data registration and the selected regions for data pair 2 (OCI: e99292015800L11N16.L1A, SeaWiFS: S1999292015126.L1B). The SeaWiFS image is shown as the background

Table 7 Results obtained by comparing the first data pair (e99159090959L11N16.L1A, S1999159091051.L1B), the selected regions are pixel_516 to pixel_584, line_528 to line_597 for OCI, and pixel_508 to pixel_531, line_940 to line_968 for SeaWiFS

OCI Band	1	2	3	4	5	6	7
$\tilde{L}^{SWF}$	3.62	3.81	3.67	3.59	3.13	1.71	3.59
$\tilde{L}_p$	13.97	11.54	9.16	11.65	1.53	0.003	9.18
α_{index}	3.86	3.03	2.50	3.22	NA	NA	2.56

However, using the above equations, $\tilde{L}_{ip}$ and $\tilde{L}_p$ are practically calculated from the data obtained by OCI, and the calculations of $\tilde{L}_i^{SWF}$ and $\tilde{L}^{SWF}$ are based on the SeaWiFS data. Thus the radiometric incompatibility between OCI and SeaWiFS unless corrected will appear in the calculation. The results of calculating (17) and (18) with the OCI and SeaWiFS data, therefore, show a combination of the incompatibility factor and gain of OCI. If the incompatibility factor is known and correctable, such as by using pre-flight cross calibration, the relative gain and gain index can be recovered. Otherwise, if the incompatibility factor is kept unchanged all the time, the gain shift of OCI can be investigated by tracking the values obtained by (17) or (18) without correction for the incompatibility. The experiments presented in the next section assume the latter case.

4. Results of Applying the Track Differential Radiance Method

With the requirements of measuring the same site near in time, three pairs of data sets acquired respectively on the 159th, 292nd, and 340th day in 1999 by OCI and the associated SeaWiFS data sets as shown in Tables 5 and 6 are picked for the cross platform comparison. To achieve data set registration, a pair of the OCI and SeaWiFS data sets are displayed by assigning Bands 670 nm, 510 nm and 443 nm to red, green and blue colors, respectively, and the two images are overlapped and aligned according to their longitude and latitude coordinates. Fig. 11 shows one of the registrations with the SeaWiFS image as the back-ground. Regions R_a and R_b are picked from the overlapping images. For applying the track differential radiance method, regions R_a and R_b are selected to be significantly different in reflectance, and no saturation occurs.

Table 8 Results obtained by comparing the second data pair (e99292015800L11N16.L1A, S1999292015126.L1B), the selected regions are pixel_236 to pixel_281, line_1275 to line_1350 for OCI, and pixel_655 to pixel_699, line_3605 to line_3611 for SeaWiFS.

OCI Band	1	2	3	4	5	6	7
$\tilde{L}^{SWF}$	4.06	4.38	4.36	4.49	3.97	2.76	4.49
$\tilde{L}_p$	14.63	12.31	11.63	14.37	5.48	3.25	12.0
α_{index}	3.60	2.81	2.67	3.20	1.38	1.18	2.67

Table 9 Results obtained by comparing the third data pair (e99340074730L11N16.L1A, S1999340074419.L1B), the selected regions are pixel_708 to pixel_733, line_885 to line_906 for OCI, and pixel_529 to pixel_532 , line_2615 to line_2639 for SeaWiFS. Since OCI operated in NI-B mode, Band 4 data is not available.

OCI Band	1	2	3	4	5	6	7
$\tilde{L}^{SWF}$	11.63	12.18	12.02	12.1	10.49	7.27	12.1
$\tilde{L}_p$	42.49	34.35	28.99	NA	13.8	10.09	36.21
α_{index}	3.65	2.82	2.41	NA	1.32	1.39	2.99

Using (18), the gain indexes and track differential radiances are obtained as listed in Tables 7 to 9. The numbers shown in bold are considered to be appropriate results. On the other hand, the track differential radiances for Bands 5 and 6 in Table 7 are relatively small compared to the noise level and the calculated gain indexes are considered to be abnormal results. Taking the results of the 159th day in 1999 (the first data set) as a base, it is found that the gain indexes of each band are almost unchanged and therefore the gains of OCI are considered to be stable. That means during the interval of data acquisition from the 159th day till the 340th day in 1999, the gains of OCI are almost unchanged. But nothing guarantees any gain is kept the same as its pre-flight value. Long-term tracking of each gain index will certainly reveal the trend of gain shift. The gain index larger than one for each Band 1 to Band 7 in Tables 7 to 9 is mainly a combination result of radiometric incompatibility and gain shift in OCI.

V. CONCLUSIONS

The reliable, compact pushbroom design of OCI has achieved a lifetime longer than its mission interval (mission ended in Jan. 2001 but it was still on duty in May 2002). However, to verify the applicability of its data, the short- and long-term variations of its optical performance should be tracked and the gain and offset for calibration-to-radiance must be corrected. In this paper, the in-flight offsets of OCI have been successfully estimated by statistically analyzing the dark night measurement data covering twenty-three months, and the band-mean offset as well as its random fluctuation showed a trend of increasing along with operation time. The bombardment of high-energy particles in the space environment is certainly the cause and will restrict the usable lifetime of OCI. Cross platform comparison between the OCI and the SeaWiFS data measured over a cross point near in time is developed to estimate the gain of OCI. Using the proposed track differential radiance method can bypass the necessity of atmospheric correction in estimating the gain. The results obtained by applying the track differential radiance method and referring to the SeaWiFS data show that the proposed approach works and the gain of OCI is stable. However, since the information of radiometric compatibility between OCI and SeaWiFS is not available, the cross platform comparison does not solve the gain of OCI directly. Instead the gain index is estimated to cover the incompatibility factor and gain shift, and the change in the gain index can indicate the gain shift in OCI.

ACKNOWLEDGMENTS

This work is one of the projects of the OCI Science Team supported by the National Space Program Office of the National Science Council under NSC-89-NSPO-A-OCI-019-01-01. The authors wish to acknowledge the ROCSAT-1 Science Data Distribution Center whose funding agency is the National Space Program Office and the work of Department of Oceanography, National Taiwan Ocean University for providing the OCI data sets.

NOMENCLATURES

CCD	Charge Coupled Devices
D	offset
$\overline{D}$	estimated offset
E^0	the spectral irradiance at the top-of-the-atmosphere
E^d	the irradiance at the earth's surface due to skylight
F_{ip}	pre-flight gain corresponding to the *i*th cell of a CCD array
g	amplification (electronic gain)

$GIFOV$	ground instantaneous field of view
L	radiance
$\tilde{L}$	differential radiance
$\tilde{L}^{SWF}$	differential radiance calculated from the SeaWiFS data
N	digital number of measured radiance
OCI	Ocean Color Imager
p	index of a pre-flight term
R_a, R_b	track segments under observation
$SeaWiFS$	Sea-viewing Wide Field-of-view Sensor
$T(x, y)$	the topological factor of the pixel
$\Delta x \times \Delta y$	effective area
α	relative gain
α_{index}	gain index
$\rho(x, y, \lambda)$	the diffuse spectral reflectance
$\tau_s(\lambda)$	the solar path atmospheric transmittance
$\tau_v(\lambda)$	the view path transmittance
λ	wavelength
$\Delta\lambda$	effective spectral band

REFERENCES

Amelio, G. F., and Dyck, R. H., 1975, "Fixed Pattern Noise and Cooled Photo-sensor Array," North Atlantc Treaty Organization Advanced Study Institute on Solid State Imaging, Universite Catholique de Louvain.

Che, N. B., Grant, B. G., Flittner, D. E., Slater, P. N., Biggar, S. F., Jackson, R. D., and Moran, M. S., 1991, "Results of Calibration of The NOAA- 11 AVHRR Made by Reference to Calibrated SPOT Imagery at White Sands, N. M." Society of Photo-Optical Instrumentation Engineers: Calibration of Passive Remote Observing Optical and Microwave Instrumentation, Vol. 1493, pp. 182-194.

Gordon, H. R., 1998, "In-flight Calibration Strategy for Ocean Color Sensors," *Remote Sensing and Environment*, Vol. 63, pp. 265-278.

Hooker, S. B., Esaias, W. E., Feldman, G. C., Gregg, W. W., and MeClain, C. R., 1992, "SeaWiFS Technical Report Series Volume 1, An Overview of SeaWiFS and Ocean Color," *Technical Memorandom* 104566, NASA, Greenbelt, MD.

Hopkinson, G. R., Dale, C. J., and Marshall, P. W., 1996, "Proton Effects in Charge-Coupled Devices," *IEEE Transactions on Nuclear Science*, Vol. 43, No. 2, pp. 614-626.

Lin, W. S., Wu, J. Y., Chiu, H. J., Chen, C. S., and Chang, Y. J., 1999, "Radiometric Characterization of the ROCSAT Ocean Color Imager," *International Journal of Remote Sensing*, Vol. 20, No. 17, pp. 3247-3263.

Narimatsu, Y., and Watanabe, F., 1997a, "Rocsat-1 Program: Ocean Color Imager FM Delivery Data Package," NEC Space Systems Division, OCI-BS-037-NEC.

Narimatsu, Y., Watanabe, F., and Suzuki, K., 1997b, "ROCSAT-1 Ocean Color Imager Calibration Report," NEC Space Systems Division, OCI-BS-039-NEC.

Ono, A., Sakuma, F., Arai, K., Yamaguchi, Y., Fujisada, H., Slater, P. N., Thome, K. J., Palluconi, F. D., and Kieffer, H. H., 1996, "Pre-flight and In-flight Calibration Plan for ASTER," *Journal of Atmospheric and Oceanic Technology*, Vol. 13, No. 2, pp. 321-335.

Rao, C. R. N., and Chen, J., 1994, "Post-launch Calibration of The Visible and Near Infrared Channels of The Advanced Very High Resolution Radiometer on NOAA-7, -9 and -11 Spacecraft," Washington D.C.: National Oceanic and Atmospheric Administration, No. NESDID 78.

Salomonson, V. V., Barnes, W. L., Maymon, P. W., Montgomery, H. E., and Ostrow, H., 1989, "MODIS: Advanced Facility Instrument for Studies of The Earth as A System," *IEEE Geoscience and Remote Sensing*, Vol. 27, pp. 145-152.

Schowengerdt, R. A., 1997, *Remote Sensing: Models and Methods for Image Processing, Academic Press*, a: pp. 310-318, b: pp. 69-94.

Slater, P. N., Biggar, S. F., Holm, R. G., Jackson, R. D., Mao, Y., Moran, M. S., Palmer, J. M., and Yuan, B., 1987, "Reflectance- and Radiance-based Methods for The In-flight Absolute Calibration of Multi-spectral Sensors," *Remote Sensing and Environment*, Vol. 22, pp. 11-37.

Yamashita, A., Dotani, T., Bautz, M., Crew, G., Ezuka, H., Gendreau, K., Kotani, T., Mitsuda, K., Otani, C., Rasmussen, A., Ricker, G., and Tsunemi, H., 1997, "Radiation Damage to Charge Coupled Devices in The Space Environment," *IEEE Transactions on Nuclear Science*, Vol. 44, No. 3, pp. 847-853.

Manuscript Received: May 17, 2002
Revision Received: Nov. 02, 2002
and Accepted: Dec. 22, 2002